

For submission to *The Astrophysical Journal*

An X-ray study of the supernova remnant G18.95–1.1

I. M. Harrus

NASA/USRA Goddard Space Flight Center, Greenbelt MD 20771

`imh@lheapop.gsfc.nasa.gov`

P. O. Slane

Harvard-Smithsonian Center for Astrophysics, Cambridge MA 02138

J. P. Hughes

Rutgers University, Piscataway NJ 08854

and

P. P. Plucinsky

Harvard-Smithsonian Center for Astrophysics, Cambridge MA 02138

ABSTRACT

We present an analysis of data from both the *Röntgen Satellite* (*ROSAT*), and the *Advanced Satellite for Cosmology and Astrophysics* (*ASCA*) of the supernova remnant (SNR) G18.95–1.1. We find that the X-ray emission from G18.95–1.1 is predominantly thermal, heavily absorbed with a column density around 10^{22} atoms cm^{-2} and can be best described by an NEI (nonequilibrium ionization) model with a temperature around 0.9 keV, and an ionization timescale of 1.1×10^{10} cm^{-3} s^{-1} . We find only marginal evidence for non-solar abundances. Comparisons between 21 cm HI absorption data and derived parameters from our spectral analysis strongly suggest a relatively near-by remnant (a distance of about 2 kpc).

Above 4 keV, we identify a small region of emission located at the tip of the central, flat spectrum bar-like feature in the radio image. We examine two possibilities for this emission region: a temperature variation within the remnant or a pulsar wind nebula (PWN). The current data do not allow us to distinguish

between these possible explanations. In the scenario where this high-energy emission region corresponds to a PWN, our analysis suggests a rotational loss rate for the unseen pulsar of about $7 \times 10^{35} \text{ erg s}^{-1}$ and a ratio L_r/L_x about 3.6 for the entire PWN, slightly above the maximum ratio (3.4 for Vela) measured in known PWN.

Subject headings: ISM: abundances – ISM: individual (G18.95–1.1) — supernova remnants — X-rays: ISM

1. Introduction

G18.95–1.1 was discovered as a non-thermal extended radio source during a continuum survey of the Galactic plane (Reich et al. 1984). The source was first suggested to be energized by a binary system containing a compact object (Fürst et al. 1985). This classification was based on the unusual radio morphology of G18.95–1.1, consisting of various arcs pointing toward a central radio peak. Follow-up radio observations (Odegard 1986) were done soon afterwards to confirm this identification. Based on a detailed analysis of the variation of the spectral index across G18.95–1.1 and on a re-analysis of the morphological characteristics used by Fürst et al. (1985), Odegard (1986) concluded that G18.95–1.1 was more likely a low surface brightness Crab-like supernova remnant (SNR) powered by a hidden central compact object, although the binary interpretation could not be completely ruled-out. He suggested further high-resolution low-frequency observations at 327 MHz to resolve the “bar-like” structure at the center of the source. Such observations were carried out by Patnaik, Velusamy, & Venugopal (1988), and their analysis yielded the detection of an almost complete shell surrounding a compact, central object. This result established that G18.95–1.1 was indeed a supernova remnant, but the origin of the energy sustaining the central emission from G18.95–1.1 remained unknown. Odegard (1986) suggested that the SNR was powered by a central pulsar. However, Fürst et al. (1989) argued that G18.95–1.1 could be a binary system consisting of the neutron star created in the supernova explosion and a low mass companion unseen because of the known large optical absorption. To solve the mystery of the energy source of the radio emission and search for a possible central object, a pointed *ROSAT* PSPC observation (12 ks) of the SNR was carried out by Fürst, Reich, & Aschenbach (1997). They found that the remnant could be best described by a thermal emission model (Raymond & Smith 1977) at a temperature of about 0.95 keV and a hydrogen column density of $3.4 \pm 1.5 \times 10^{21} \text{ atoms cm}^{-2}$. A non-thermal model (power-law) yielded a photon index of $\alpha = -8.9$ which was therefore dismissed as an “unrealistic” model. In addition to the X-ray data, Fürst, Reich, & Aschenbach (1997) obtained a detailed radio

map (at an angular resolution of $69''$) using the Effelsberg 100-m telescope at 10.55 GHz where Faraday depolarization effects are small. The image extracted from these data is shown in Figure 1¹. It shows a distinct central bar surrounded by a faint shell of diffuse emission. About 80% of the radio emission is in the central diffuse component and has a total flux of about 20.4 ± 0.2 Jy at 10.55 GHz. This result is consistent with existing radio data at 1.4 GHz and 4.75 GHz for a spectral index ($S_\nu \propto \nu^\alpha$) $\alpha = -0.14 \pm 0.03$ for the diffuse component and $\alpha = -0.22 \pm 0.07$ for the central bar. A prominent arc on the western part of the remnant (see Figure 1) has a steeper spectral index of $\alpha = -0.36 \pm 0.04$. The linear polarization across the remnant is about 6% at 10.55 GHz, a little more than twice that at 4.75 GHz. The polarization intensity is highly concentrated on small scales: when the diffuse contribution is subtracted, the polarization increases to about 40% in the central bar and in the arc.

As is often the case in SNR studies, the distance to G18.95–1.1 is not well known. There exist 21 cm HI absorption data (Braunsfurth & Rohlfs 1984) which were re-analyzed by Fürst et al. (1989). Based on a radial velocity of 18 km s^{-1} associated with G18.95–1.1, they deduced a distance of either 2 kpc (within the Sagittarius arm) or 15 kpc (on the far side of the Galaxy). Because of the large luminosity and velocity expansion implied by this latter distance, they considered the closer distance as the most probable and derived all physical quantities using a 2 kpc measure to the SNR. We will derive all our results normalized to this distance unless otherwise specified and we comment at the end of the paper on the possibility that the remnant is as far away as 15 kpc.

Our motivation, in starting the following investigation of the SNR G18.95–1.1 was to solve, once and for all, the mystery of the energy source of the emission from the remnant, namely: was a compact object powering the emission of the remnant? In view of the *ASCA* data, we have reanalyzed the existing *ROSAT* PSPC data, an analysis we present in §2. In §3 we describe the data extraction methods, and the spatial and spectral analysis of the *ASCA* data. In §4 we discuss the implications of our analysis and a summary of our principal conclusions.

2. Analysis of the *ROSAT* PSPC data

We extracted the G18.95–1.1 *ROSAT* PSPC data from the public archive and processed them to minimize the contribution from the particle background (Snowden et al. 1994). There is no *ROSAT* HRI observation of this remnant. A point source, also mentioned

¹The data were kindly provided by Professor Fürst at the Max-Planck-Institute für Radioastronomie.

in Fürst, Reich, & Aschenbach (1997), is detected within the boundary of the SNR at $18^{\text{h}}28^{\text{m}}48^{\text{s}}$, $-13^{\circ}00'55''$ (J2000). The source was not definitely identified by Fürst, Reich, & Aschenbach (1997) and it has no radio counterpart. This point source is positionally coincident (given the star’s known proper motion and the position accuracy of the *ROSAT* PSPC) with a star identified in 2MASS at a position of $18^{\text{h}}28^{\text{m}}50.08^{\text{s}}$, $-13^{\circ}01'20.3''$ (J2000). We consider the likelihood that this is the counterpart to the X-ray source in more detail below.

For our *ROSAT* PSPC spectral analysis of the entire remnant, we have extracted data from a $17'$ radius circle (the extent of the remnant). In the first part of our analysis, we have modeled the thermal emission with collisional ionization equilibrium (CIE) models, the so-called *mekal* model (Mewe, Gronenschild, & van den Oord 1985; Mewe, Lemen, & van den Oord 1986; Kaastra 1992) and the so-called *raym* model (Raymond & Smith 1977) which are available in XSPEC v11.2, the X-ray spectral analysis package used throughout this analysis. In all the thermal models used, unless explicitly specified, we have kept the elemental abundances at their solar values as derived by Anders & Grevesse (1989). Absorption along the line of sight was taken into account with an equivalent column density of hydrogen, N_{H} , using the cross-sections and abundances from the Balucinska-Church & McCammon (1992) photo-electric absorption model. In agreement with existing results we found that a single component thermal model can describe the data with a temperature around 0.3 keV and a hydrogen column density around 10^{22} atoms cm^{-2} for all the thermal models used in this analysis. We examined non-equilibrium ionization (NEI) effects arising when the ions are not instantaneously ionized to their equilibrium configuration at the temperature of the shock front (Gronenschild, & Mewe 1982). To incorporate these effects into the model of SNR spectral emissivity, we use here the *pshock* model incorporated in XSPEC (Borkowski et al. 2001). This model incorporates the Fe-L shell atomic data computation from Liedahl, Osterheld, & Goldstein (1995) and it is a first approximation to the physical phenomena which occurs at the shock. It does not include radiative and di-electronic recombinations, nor any coupling between ions and electrons, but despite its shortcomings (present in most of the other models available), the model is useful to provide a good first approximation of the physical state of the plasma. The ionization state depends on the product of the electron density and the age, and we define the ionization timescale as $\tau_i \equiv n_e t$. The larger the value of the ionization timescale, the closer the system is to ionization equilibrium (Gronenschild, & Mewe 1982). When fitted with such a model, the data lead to a similar, although slightly smaller, column density (7×10^{21} atoms cm^{-2}) but at a much higher temperature (3.3 keV) and an ionization timescale ($n_e t = \tau_i = 2.3 \times 10^{10}$ cm^{-3} s) far from the equilibrium value ($n_e t$ at equilibrium is larger than 10^{12} cm^{-3} s). As found by Fürst, Reich, & Aschenbach (1997), a non-thermal (power-law type) model does not fit the data as well and the value of

the spectral index found in this case ($\alpha > 7.5$) is unphysically large. All fits (thermal and non-thermal) imply a large value of the absorption column density (close to 10^{22} atoms cm^{-2}).

3. *ASCA* Analysis

With a diameter of about $33'$, G18.95–1.1 could not be entirely covered with the *ASCA* SIS in the standard 2 CCDs mode (the GIS covers the remnant almost completely.) We chose to cover overlapping but different parts of the remnant with the two SIS detectors. The resulting field of view is a characteristic L-shaped image, the overlapping CCDs covering the region of the point source identified by *ROSAT*. We used the standard processed data as provided by the *ASCA* Guest Observer Facility². The event processing configuration was kept at its default value, with a GIS time resolution of 0.125 s (the SIS is not used for timing analysis).

3.1. Spatial

We generated exposure-corrected, background-subtracted images of the GIS and SIS data in soft (below 4.0 keV) and hard (above 4.0 keV) energy bands for the ~ 25 ks observation.³ We used newly generated blank maps to estimate the background. These maps, available only for the GIS, are more complete than the standard “high latitude” ones used in similar studies. They were first corrected for spurious point sources and then screened using the standard event screening criteria⁴. We used the standard “blank maps” for the SIS. Exposure maps (both for GIS and SIS) were generated using the *ascaeffmap* and *ascaexpo* scripts⁵. Events from regions of the merged exposure map with less than 30% of the maximum exposure were ignored. Merged images of the source data, background, and exposure were smoothed with a Gaussian of standard deviation, $\sigma = 45''$. We subtracted smoothed background maps from the data maps and divided by the corresponding exposure map. Figure 2 shows the results of this procedure for both the SIS and the GIS detectors

²See the “Guide for *ASCA* data reduction” at http://heasarc.gsfc.nasa.gov/docs/asca/ahp_proc_analysis.html for more information on the cuts applied to the data.

³We used here a new *ASCA* FTOOLS package called *fmosaic*.

⁴For more details on the generation of these files, see <http://heasarc.gsfc.nasa.gov/docs/asca/mkgisbgd/mkgisbgd.html>.

⁵Both scripts are part of the *ASCA* FTOOLS package <http://heasarc.gsfc.nasa.gov/docs/software/ftools/asca.html>.

at energies below and above 4 keV. The GIS low-energy image, covering almost all of the remnant, shows two maxima of emission located respectively at $18^{\text{h}}29^{\text{m}}15.6^{\text{s}}$, $-12^{\circ}55'22.5''$ and $18^{\text{h}}28^{\text{m}}49.9^{\text{s}}$, $-13^{\circ}01'7.44''$ (2000). There is evidence for emission above 4 keV in the GIS (a signal-to-noise ratio at the peak of about 4). This emission is centered at $18^{\text{h}}29^{\text{m}}4.3^{\text{s}}$, $-12^{\circ}52'33.7''$ and is confined to a small region (a little less than $3'$ in radius, comparable to the PSF of the instrument). The SIS does not cover this part of the remnant. We show in Figure 3 an overlay of the soft X-ray contours on the 30 GHz radio image with the location of the hard X-ray source marked by the small white circle. As seen in this picture, while the remnant's extent is slightly smaller in the X-ray band than in the radio, the central region shows obvious correlations in the emission morphology at both frequencies. The central radio bar overlaps almost entirely with the central low energy X-ray emission, and the maximum of the higher energy emission is located at the tip of that bar.

3.2. Spectral

We first studied the integrated emission from the remnant by extracting the X-ray spectra from the GIS data from a circular region centered at $18^{\text{h}}29^{\text{m}}23.72^{\text{s}}$, $-13^{\circ}00'44.76''$ (J2000) and using a radius of $11'7.4''$, chosen to encompass most of the emission from the SNR. This region covers almost the entire extent of the remnant in the *ROSAT* pointing, making a direct comparison between the two datasets possible. We extracted the background from regions in the GIS field of view free of emission from the remnant. Because the detector in the L-shaped configuration of the SIS does not cover the complete remnant, in the following analysis, we have used the SIS data exclusively in the study of the point source detected in the *ROSAT* observation. The measured count rates are 0.465 ± 0.006 cnt s $^{-1}$ for the complete remnant (as measured with the GIS) and 0.039 ± 0.001 cnt s $^{-1}$ (0.042 ± 0.001 cnt s $^{-1}$) for the point source in the GIS (SIS). Our spectral analysis is divided into several parts. We first study the complete remnant, then examine in detail the high-energy emission region detected above 4 keV in the GIS. We then analyze the data from the star and finally from the small part of the remnant where the radio emission is the strongest. All detailed results are given in Tables 1 & 2.

We extracted the *ASCA* GIS spectrum of the entire remnant (a total of 18600 events). The gain offset was allowed to vary, and we measured a gain shift of -3.2% and a range of variation between -2.6% and -3.6%. This gain adjustment is consistent with the results from the calibration data analysis done by the *ASCA* GIS team⁶. We used a pure thermal

⁶see http://heasarc.gsfc.nasa.gov/docs/asca/ahp_proc_analysis.html for more information on calibration.

(CIE “mekal”) model to describe the emission and obtained a χ^2 of 124.9 and a reduced χ^2 (χ_r^2) of 1.92. We found a column density of $9.8 \pm 0.5 \times 10^{21}$ atoms cm^{-2} , completely consistent with the value derived from our *ROSAT* analysis. The temperature is $kT = 0.62 \pm 0.03$ keV. The unabsorbed flux in the [0.5-2.0] keV range is between 1.9 and 2.5×10^{-10} ergs cm^{-2} s^{-1} , about three orders of magnitude higher than the contribution in the [4.0-10.0] keV band. We then fitted the *ASCA* GIS and *ROSAT* PSPC spectra simultaneously (the gain offset in the GIS was fixed to the value derived from the single GIS fit alone) as *ROSAT* PSPC data provide a stronger constraint on the column density value. We found $8.4 \pm 0.3 \times 10^{21}$ atoms cm^{-2} associated with a similar temperature ($kT = 0.58^{+0.02}_{-0.04}$ keV), very much consistent with the results found with the *ASCA* GIS alone. As in the analysis of the *ROSAT* PSPC, we examine nonequilibrium ionization effects using the *pshock* model (Borkowski et al. 2001) described in the previous section. As in the CIE model, all elements are kept to their solar abundances as defined by Anders & Grevesse (1989) except when explicitly specified. The gain adjustment for the *ASCA* GIS data is set to the same value as the one found in the CIE analysis. While we recognize that this is not formally correct (because NEI effects shift the line centroids relative to what is expected for a CIE model, precisely what our correction does), it is a reasonable approximation (the shift between the CEI and NEI models is on the order of 1% at Si-K, smaller than the gain shifts found in our analysis). A combined fit with the *ASCA* GIS and the *ROSAT* PSPC leads to a hydrogen column density $9.4^{+0.03}_{-0.10} \times 10^{21}$ atoms cm^{-2} consistent with the value found in the CIE fit. The associated temperature of $0.9^{+0.4}_{-0.1}$ keV is above the equilibrium value found in the previous analysis. This temperature from the NEI fit is associated with a low ionization timescale of $(1.35^{+1.44}_{-0.16}) \times 10^{10}$ cm^{-3} s. The fit is significantly better than the one done using the equilibrium model (a drop in χ^2 of more than 100 with the addition of one more degree of freedom) and this is the result that we will use in our analysis section. The results of all the fits are given in Table 1 and Figure 4 shows the result of the best *pshock* fit. We have searched for possible deviations from solar abundance in the spectrum of the remnant. Any such variations could be the sign of either ejecta from the supernova explosion or anomalous abundances in the interstellar medium swept-up by the expanding blast wave. We find that departures from solar abundance for Mg, Si and S are not significant at the 90% confidence level (CL). When allowed to vary, the Mg abundance increases by about 50% with a drop in χ^2 of about 30, and the S abundance decreases to a very small value for a drop in χ^2 of about 15. The associated column density, temperature, and ionization timescale are either identical or compatible at the 90% CL with the values found in the previous analysis. We find a similar but somewhat less significant result (a much smaller drop in χ^2) for the Si abundance.

We then analyzed the region of the high-energy emission. We first extracted, for compar-

ison, the spectrum from a region showing no sign of high-energy emission. We chose a circle of about $2'$ radius and centered at $18^{\text{h}}29^{\text{m}}28.935^{\text{s}}$, $-13^{\circ}03'52.47''$ (J2000). The extracted spectrum from this region (a total of 690 events) is compatible with the results found for the whole remnant. We find that with the column density fixed to the value derived in the previous analysis, the temperature of this region is in the range $0.5 - 1.6$ keV and $n_e t$ is essentially unconstrained. This poor precision is due to the small number of events in the spectrum. We then extract the spectrum from a similar size region centered at $18^{\text{h}}29^{\text{m}}4.3^{\text{s}}$, $-12^{\circ}53'33.7''$ (J2000) and used both the model derived from the study of the "comparison" region (with an arbitrary normalization value) and an additional model intended to characterize the excess emission at high-energy. The low-energy flux from the first region was used to normalize the underlying contribution of the rest of the remnant. We find that, due mainly to the poor statistics on this spectra – a total of 891 events, the excess X-ray high-energy emission cannot be characterized uniquely. Both thermal and non-thermal models can describe the data with a χ_r^2 around 2. In these two component models the column density is fixed to the value derived for the complete remnant (9.4×10^{21} atoms cm^{-2}). We find that a thermal model for the extra emission implies a relatively high temperature (a best fit at $2.1_{-1.0}^{+7.5}$ keV for a Mekal model). There are several tentative explanations for a small high-temperature region within a remnant. It could be a region of lower density shock-heated plasma, which assuming pressure equilibrium would produce a higher measured temperature than elsewhere in the remnant. In principle, one could distinguish between different regions of emission but *ASCA* lacks the necessary spatial resolution. A small region of ejecta material would be another possible explanation for a temperature variation on that scale. *ASCA*'s shortcoming in this case, is its spectral resolution, too poor to identify abundance variation with the existing statistics. It could also be that the high-energy emission detected in the remnant is powered by a hidden pulsar. In this case, one would expect a non-thermal spectrum, the expected signature of the synchrotron emission from electrons accelerated in the nebula surrounding a pulsar. We find that for a non-thermal power law model of the emission, the power law index for the best fit is $2.9_{-1.1}^{+1.6}$ (at 90% CL). This is a bit larger than the canonical value but the large error bars associated with this result preclude any definitive conclusion.

We also studied the characteristics of the X-ray emission centered around the point source detected in the *ROSAT* and *ASCA* GIS and SIS data. We extracted the X-ray spectrum from a region centered at $18^{\text{h}}28^{\text{m}}49.9^{\text{s}}$, $-13^{\circ}01'7.44''$ (J2000), the maximum of emission in the *ROSAT* PSPC image. We find that the spectra (both *ROSAT* PSPC and *ASCA* SIS) can be best described by a thermal model (CIE) at a temperature of 0.55 ± 0.10 keV and a column density of $9.2_{-1.1}^{+1.3} \times 10^{21}$ atoms cm^{-2} consistent with the results of the general fit ($\chi_r^2 = 1.18$). As mentioned above, this source is coincident with a star in the 2MASS and USNO-B1 catalogues. The observed infrared magnitudes from 2MASS are $J=9.854 \pm 0.027$,

$H=9.444\pm0.036$, and $K=9.323\pm0.028$. The star (5698-00714-1 in USNO-B1) has optical magnitudes of $B=11.60\pm0.22$ and a $V=11.58\pm0.15$. We used the measured X-ray column density to deduce a reddening of $A_V=5.14^{+0.72}_{-0.61}$ Predehl et al. (1995), which results in dereddened magnitudes of B_0 , V_0 , J_0 , and K_0 of 4.85, 6.44, 8.27, and 8.60 respectively. The resulting $(B-V)_0$ color of 1.58 is inconsistent with any main sequence, giant, or supergiant stellar candidate, casting doubt on the identification of this star as the optical counterpart to the X-ray source. A much lower value of $A_V \sim 1$ is required to make the colors compatible with an early-type star. However our X-ray analysis clearly rejects a low column density; the lower limit allowed at 90% confidence is 8.1×10^{21} atoms cm^{-2} ($A_V \sim 4.5$). The definitive identification of the optical counterpart remains elusive.

Finally, we also extracted a spectrum from the region of the brightest radio emission and the largest polarization and compared our results with those obtained from the analysis of the complete remnant. The spectral extraction region was about $4'$ in radius and centered at $18^{\text{h}}29^{\text{m}}17.16^{\text{s}}$, $-12^{\circ}53'52.20''$ (J2000). The spectrum has fewer than 900 events and we find that within the uncertainties, the X-ray emission from this region is indistinguishable from the rest of the remnant. The values obtained for the hydrogen column density and the temperature are consistent with those found for the rest of the remnant. Quantitative results and fluxes are tabulated in Table 2.

4. Discussion

As mentioned at the beginning of this paper, the distance to G18.95–1.1 is not well known and we use the lower distance estimate (2 kpc) derived from 21 cm HI absorption data (Braunsfurth & Rohlfs 1984; Fürst et al. 1989). At this distance, the supernova remnant defines an X-ray emitting volume of $V \simeq 1.2 \times 10^{59} f D_2^3 \theta_{17}^3 \text{ cm}^{-3}$, where f is the volume filling factor of the emitting gas within the SNR, and θ_{17} the angular radius in units of $17'$. Because of the large variations in the spectral results using both the standard CIE model and our *pshock* NEI analysis, all the following results were computed using error bars twice as large as that found in the analysis. This allows us to gauge more effectively the different evolution scenarios for G18.95–1.1 while acknowledging the difficulty in reaching definitive conclusions with these data alone. We deduce a hydrogen number density $n_{\text{H}} = (0.13 - 0.24) D_2^{-1/2} \theta_{17}^{-3/2} f^{-1/2} \text{ cm}^{-3}$. The mass of the X-ray emitting plasma M_X , is $(17 - 31) D_2^{5/2} f^{1/2} \theta_{17}^{3/2} M_{\odot}$. At a distance of 15 kpc this would imply a mass of $3000 M_{\odot}$, for a Taylor-Sedov value of 0.25 for the filling factor f (Taylor 1950; Sedov 1959). With the preceding numerical values we estimate the supernova explosion energy E to be $(0.4 -$

$0.9) \times 10^{50} D_2^{5/2} \theta_{17}^{3/2} f^{-1/2}$ ergs. For a nominal value of f and at 2 kpc, E is within (although on the low side) standard values for SN explosions. We note that this value is derived under the hypothesis that electrons and ions are in temperature equilibrium (a simplification that may not be correct in this case) and that a larger explosion energy is allowed if the ions are substantially hotter than the electrons. An estimate of the age of the remnant can be made using our spectral analysis results. We found t between 4400 and 6100 yr, where the range reflects the uncertainties in the fit, but does not include any error on the distance (assumed at 2 kpc) – the age varies linearly with the distance. The preshock ISM number density is $n_0 \sim \rho_0/m_H = (0.06 \pm 0.02) D_2^{-1/2} \theta_{17}^{-3/2} f^{-1/2} \text{ cm}^{-3}$. As noted in the introduction, 21 cm HI absorption data (Braunsfurth & Rohlfs 1984; Fürst et al. 1989) do not exclude a distance of 15 kpc to G18.95–1.1. If we compute the physical characteristics that this distance would imply for the remnant, we find an explosion energy larger than $E = 2 \times 10^{52}$ ergs, one order of magnitude larger than the value derived from the current SN explosion models. In addition, because of the large swept-up mass derived in that case, we argue that the results from our X-ray analysis actually rule out this distance. Based on the radio data alone, it is not surprising that G18.95–1.1 was suspected to harbor a compact object. As described in the spectral analysis summarized above (see §3), the X-ray emission does provide some clues to the real nature of the emission. The X-ray emission from the remnant is clearly dominated by thermal emission and we argue that the remnant is in non-equilibrium ionization, a hypothesis compatible with the age (between 4400 and 6100 yr) derived in the context of this model. Our data reveal a clear region of high-energy emission (above 4 keV) located at the tip of the radio bar, although our spectral analysis does not lead to a definitive answer as to the origin of this emission. We have examined two hypotheses. In the first scenario, this emission results from a high-energy nebula powered by a hidden pulsar. Our X-ray analysis yields a non-thermal X-ray unabsorbed flux of about $7 \times 10^{32} \text{ erg s}^{-1}$ between 0.2 and 4 keV or about 0.7% of the flux from the rest of the remnant. This, in turn, suggests a rotational energy loss \dot{E} of about $7 \times 10^{35} \text{ erg s}^{-1}$ (Seward & Wang 1988; Becker & Trümper 1997). By comparison, this value is about twice that of the pulsar/SNR in W44 whose pulsar’s luminosity is about 1% that of the total remnant (Harrus, Hughes, & Helfand 1996). We computed the radio luminosity associated with the region from which the high-energy emission is coming and we find about $2.5 \times 10^{33} \text{ erg s}^{-1}$ at a distance of 2 kpc and using the spectral index from the bar $\alpha = -0.22$ given in Fürst, Reich, & Aschenbach (1997). This value leads to a ratio L_r/L_x about 3.6, a bit larger than measured values for other PWNe (that ratio varies from 3.4 for Vela to 3.2×10^{-4} for MSH 15-52).

We have presented the results of *ROSAT* and *ASCA* X-ray spectral and spatial studies of the SNR G18.95–1.1, a middle-aged SNR (about 5000 yr old) most probably in its Taylor-Sedov phase of evolution and at a distance of 2 kpc. The remnant is best described by a

nonequilibrium ionization model with solar elemental abundances. There are several X-ray bright spots in the remnant that are generally consistent with thermal emission. We find that we cannot make a definitive identification of the optical counterpart to the unresolved *ROSAT* PSPC X-ray source. The nature of an unresolved hard *ASCA* X-ray source located near the tip of the central radio bar remains enigmatic. Future Chandra and XMM-Newton observations may shed more light on this question.

Our research made use of data obtained from the High Energy Astrophysics Science Archive Research Center Online Service, provided by the NASA Goddard Space Flight Center. This publication makes use of data products from the Two Micron All Sky Survey, which is a joint project of the University of Massachusetts and the Infrared Processing and Analysis Center, funded by the National Aeronautics and Space Administration and the National Science Foundation. This research has also made use of the USNOFS Image and Catalogue Archive operated by the United States Naval Observatory, Flagstaff Station (<http://www.nofs.navy.mil/data/fchpix/>). IMH acknowledges support through NASA grants NAG5-8394. POS acknowledges support through NASA contract NAS8-39073 and grant NAG5-9281. IMH would like to thank Steve Drake for his help in navigating the intricacies of star catalogues.

REFERENCES

- Anders, E., & Grevesse, N. 1989, *Geochim. Cosmochim. Acta*, 53, 197
- Balucinska-Church, M. & McCammon, D. 1992, *ApJ*, 400, 699
- Becker, W. & Trümper, J. 1997 *A&A*, 326, 682
- Borkowski, K. J., Lyerly, W. J., & Reynolds, S. P. 2001, *ApJ*, 548, 820
- Braunsfurth, E. & Rohlfs, K. 1984, *A & AS*, 57, 189
- Fürst, E., Reich, W., & Aschenbach, B. 1997, *A&A*, 319, 655
- Fürst, E., Hummel, E., Reich, W., Sofue, Y., Sieber, W., Reif, K., & Dettmar, R. J. 1989, *A&A*, 209, 361
- Fürst, E., Reich, W., Reich, P., Sofue, Y., & Handa, T. 1985, *Nature*, 314, 720
- Gronenschild, E. H. B. M., & Mewe, R. 1982, *A&AS*, 48, 305

- Harrus, I. M., Hughes, J. P., & Helfand, D. J. 1996, ApJ, 464, L161
- Kaastra, J. S. 1992, An X-Ray Spectral Code for Optically Thin Plasmas, Internal SRON-Leiden Report, updated version 2.0
- Liedahl, D. A., Osterheld, A. L., & Goldstein, W. H. 1995, ApJ, 438, L115
- Mewe, R., Gronenschild, E. H. B. M., & van den Oord, G. H. J. 1985, A&AS, 62, 197
- Mewe, R., Lemen, J. R., & van den Oord, G. H. J. 1986, A&AS, 65, 511
- Odegard, N. 1986, AJ, 92(6), 1372
- Patnaik, A. R., Velusamy, T., & Venugopal, V. R., 1988, Nature, 332, 136
- Predehl, P. , & Schmitt, J. H. M. M. 1995, A&A, 293, 889
- Raymond, J. C., & Smith, B. W. 1977, ApJS, 35, 419
- Reich, W., Fürst, E., , Steffen, P., Reif, K. & Haslam, C., G., T. 1984, A&AS, 58, 197
- Sedov, L. I. 1959, Similarity and Dimensional Methods in Mechanics, (New York: Academic)
- Seward, F. D. & Wang, Z.-R. 1988, ApJ, 332, 199
- Snowden, S. L., McCammon, D., Burrows, D. N., & Mendenhall, J. A. 1994, ApJ, 424, 714
- Stocke, J. T., Morris, S. L., Gioia, I. M., Maccacaro, T., Schild, R., Wolter, A., Fleming, T. A., & Henry, J. P. 1991, ApJS, 76, 813
- Taylor, G. I. 1950, Proc Royal Soc London, 201, 159

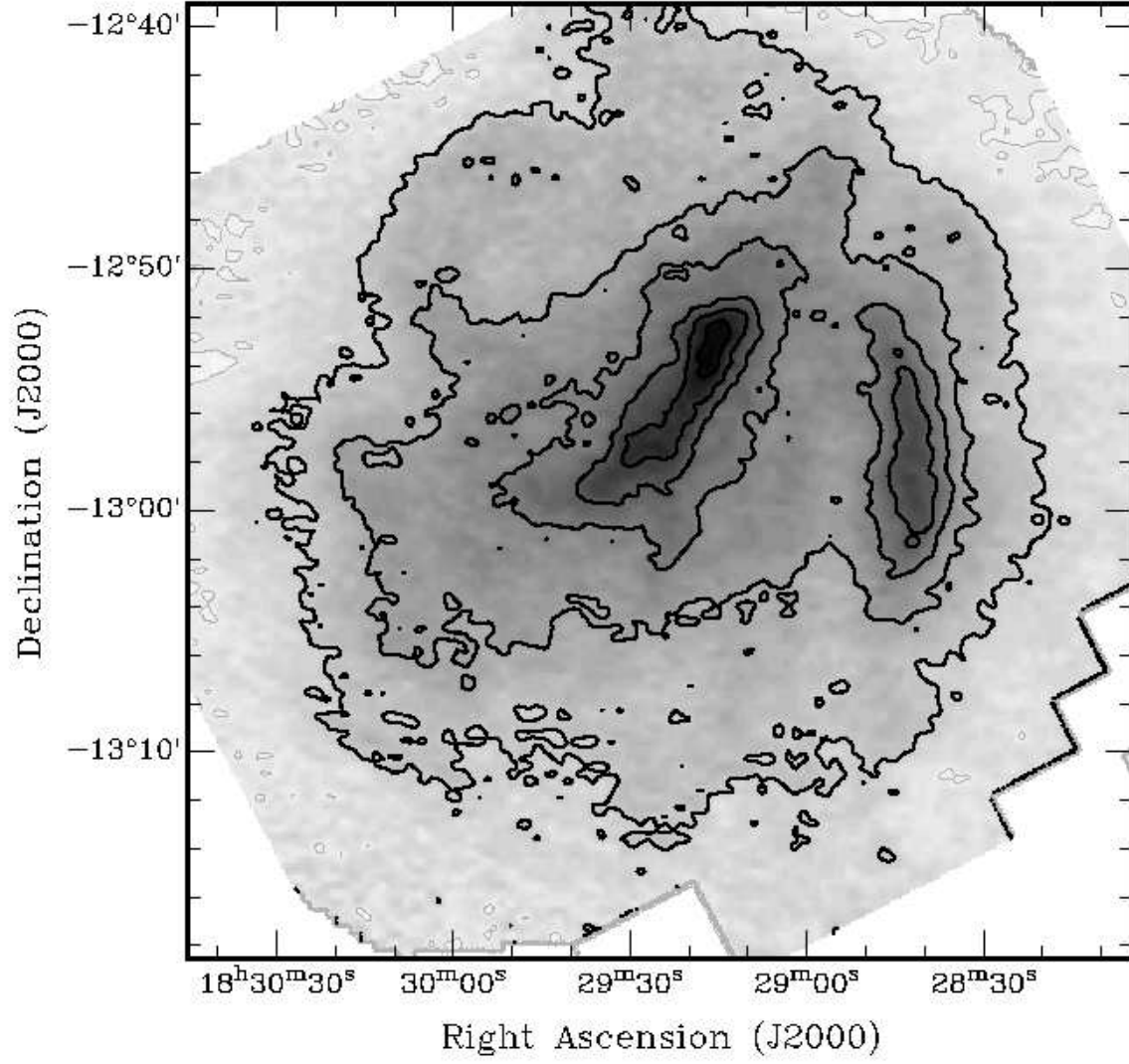


Fig. 1.— The radio contour map of G18.95–1.1 at 10.55 GHz (image provided by Dr. Fürst). The peaked intensity located at $18^{\text{h}}29^{\text{m}}16.08^{\text{s}}$, $-12^{\circ}53'12.7''$ is about 91 mJy. The remnant extent is about 17' in radius.

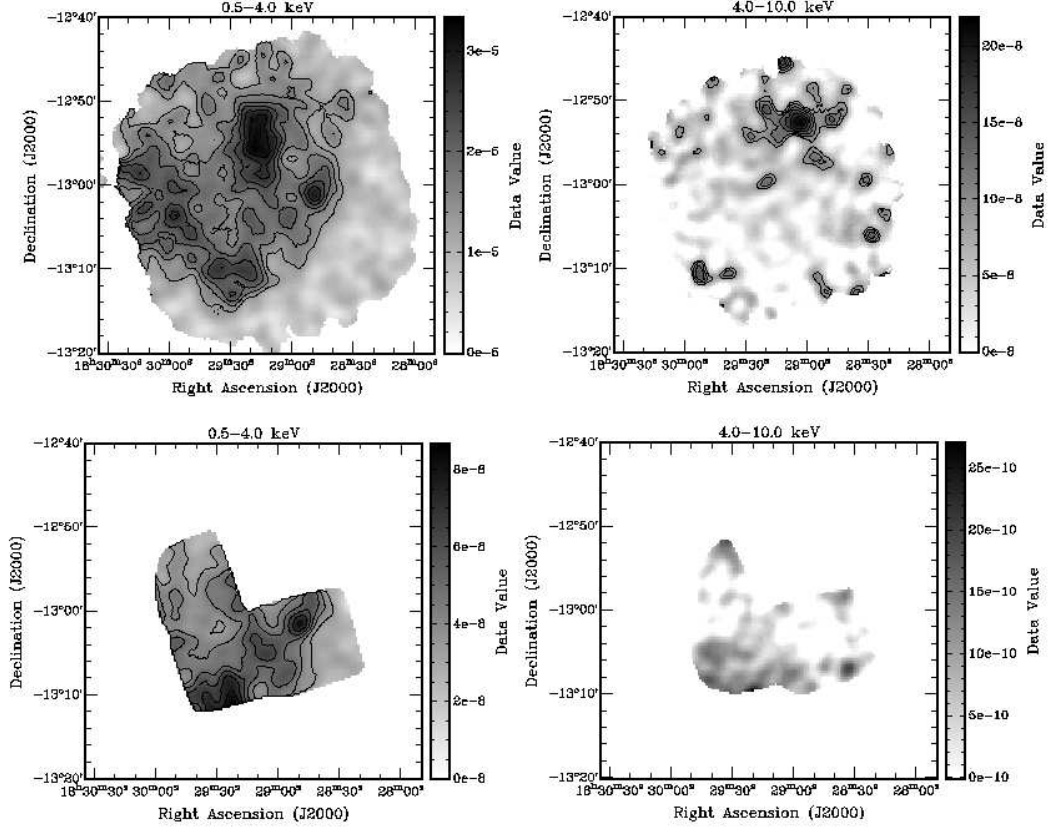


Fig. 2.— *ASCA* X-ray images of the SNR G18.95–1.1 at low energy and high energy (0.5–4.0 keV and 4.0–10.0 keV) for the GIS (upper images) and the SIS (lower images). We display only 6 linearly spaced contours, varying from 40% to 90% of the peak surface brightness in each map. The Peak/Background values are 4.2/0.7 (0.02/0.005) for the GIS at low (high energy). The similar value for the SIS are 7.5/1.6 at low energy (no high energy emission is detected in the SIS.) All values are quoted in units of $10^{-3}\text{cnt s}^{-1} \text{arcmin}^{-2}$. The bar on the left indicate the values associated with each maps in unit of $\text{cnt s}^{-1} \text{pixel}^{-1}$.

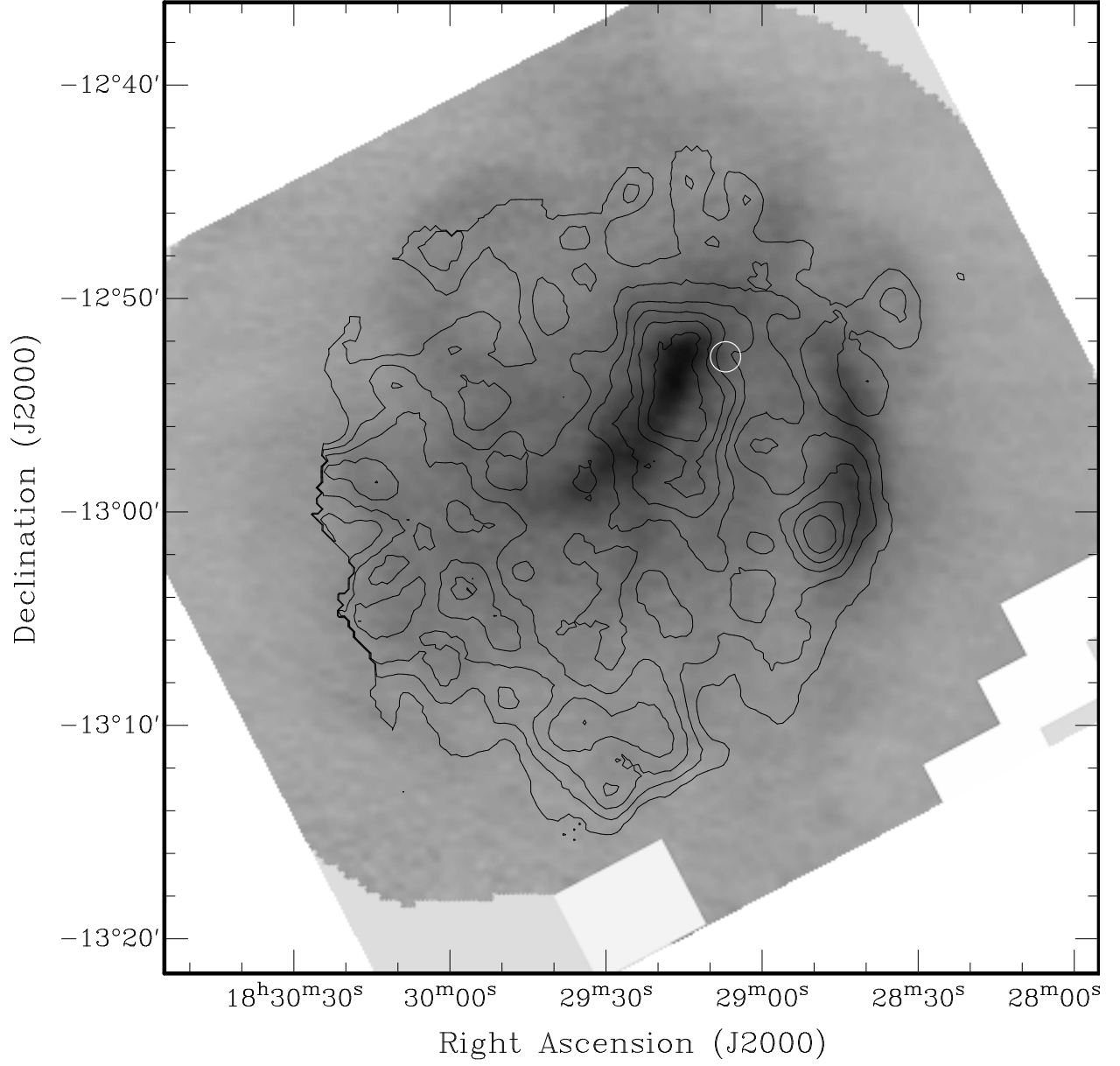


Fig. 3.— Radio image extracted from the Galactic Plane survey at 10.55 GHz (image provided by Dr. Fürst), shown with contours derived from *ASCA* GIS images at low energy (0.5–4.0 keV). The position of the maximum of the high energy emission is marked by a small white circle.

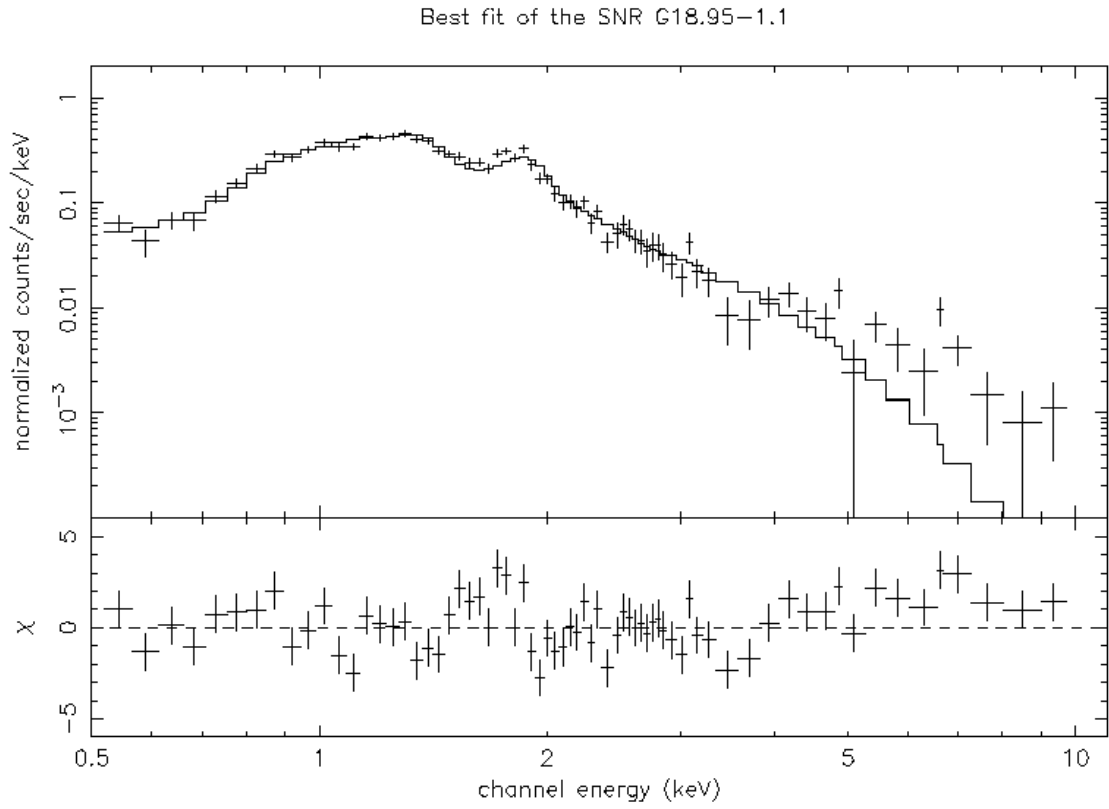


Fig. 4.— *ASCA* GIS spectra of G18.95–1.1 extracted from a $11.1'$ radius circular region. The solid curve in the top panel shows the best-fit using the *pshock* model (Borkowski et al. 2001). The bottom panel shows the data/model residuals.

Table 1.
Results from the Spectral Analysis
Complete remnant (GIS and *ROSAT* PSPC)

Parameter	CIE thermal model ^a	NEI thermal model	NEI thermal model variable Mg, Si, S abundances
N_H (atoms cm^{-2})	$8.4 \pm 0.3 \times 10^{21}$	$9.4^{+0.03}_{-0.10} \times 10^{21}$	$8.3^{+0.4}_{-0.5} \times 10^{21}$
kT (keV)	$0.58^{+0.02}_{-0.04}$	$0.9^{+0.4}_{-0.1}$	$1.12^{+0.11}_{-0.16}$
$\log(n_e t)$ ($\text{cm}^{-3} \text{ s}$)	N/A	$10.13^{+0.31}_{-0.06}$	$10.15^{+0.11}_{-0.09}$
Normalization(cm^{-5}) ^b GIS	$(7.7\text{--}9.3) \times 10^{12}$	$(4.7\text{--}13.7) \times 10^{12}$	$(4.2\text{--}8.4) \times 10^{12}$
Normalization(cm^{-5}) Rosat	$(5.2\text{--}6.2) \times 10^{12}$	$(3.2\text{--}9.1) \times 10^{12}$	$(2.8\text{--}5.6) \times 10^{12}$
Flux (ergs $\text{cm}^{-2} \text{ s}^{-1}$) ([0.5 – 2.0] keV)	$(2.0\text{--}2.4) \times 10^{-10}$	$(0.5\text{--}1.5) \times 10^{-9}$	$(4.6\text{--}5.6) \times 10^{-10}$
Flux (ergs $\text{cm}^{-2} \text{ s}^{-1}$) ([2.0 – 4.0] keV)	$(3.3\text{--}4.5) \times 10^{-12}$	$(0.2\text{--}1.8) \times 10^{-11}$	$(2.8\text{--}5.7) \times 10^{-12}$
Flux (ergs $\text{cm}^{-2} \text{ s}^{-1}$) ([4.0 – 10.0] keV)	$(0.67\text{--}1.4) \times 10^{-13}$	$(0.1\text{--}3.4) \times 10^{-12}$	$(0.32\text{--}1.10) \times 10^{-12}$
Mg/Mg $_{\odot}$	1	1	1.5 ± 0.2
Si/Si $_{\odot}$	1	1	$1.4^{+0.4}_{-0.3}$
S/S $_{\odot}$	1	1	$0.4^{+0.6}_{-0.4}$
χ^2/ν	$283.8/90 = 3.15$	$157.2/89 = 1.76$	$116.8/86 = 1.36$

^a Single-parameter 1 σ errors

^b $N = (\frac{n_H n_e V}{4\pi D^2})$

Table 2.

Parameter	Radio bright region (GIS)	Radio bright region (GIS)	Rest of the remnant (GIS)
	CIE thermal model	NEI thermal model	NEI thermal model
N_H (atoms cm^{-2})	$1.6 \pm 0.4 \times 10^{22}$	$0.6^{+0.4}_{-0.3} \times 10^{22}$	$0.88^{+0.09}_{-0.04} \times 10^{22}$
kT (keV)	$0.30^{+0.12}_{-0.06}$	$0.50^{+0.3}_{-0.1}$	$0.80^{+0.4}_{-0.1}$
$\log(n_e t)$ ($\text{cm}^{-3} \text{ s}$)	NA	≤ 10.33	≥ 11.02
Normalization(cm^{-5})	$(1.4\text{--}14.4) \times 10^{12}$	$(0.9\text{--}7.6) \times 10^{12}$	$(1.6\text{--}3.5) \times 10^{12}$
Flux (ergs $\text{cm}^{-2} \text{ s}^{-1}$) ([0.5 – 2.0] keV)	$(0.22\text{--}3.3) \times 10^{-10}$	$(0.01\text{--}7.7) \times 10^{-10}$	$(4.5\text{--}7.3) \times 10^{-11}$
Flux (ergs $\text{cm}^{-2} \text{ s}^{-1}$) ([2.0 – 4.0] keV)	$(0.01\text{--}2.3) \times 10^{-12}$	$(0.02\text{--}3.6) \times 10^{-12}$	$(1.0\text{--}7.2) \times 10^{-12}$
Flux (ergs $\text{cm}^{-2} \text{ s}^{-1}$) ([4.0 – 10.0] keV)	$(0.0006\text{--}1.8) \times 10^{-14}$	$(0.001\text{--}2.2) \times 10^{-13}$	$(0.4\text{--}11.7) \times 10^{-13}$
χ^2/ν	$33.22/27 = 1.23$	$23.00/26 = 0.88$	$265/135 = 1.95$